Original Article

DOI: 10.5582/bst.2026.01117

Clinically constrained optical design of a high-numerical aperture miniature immersion objective for probe-based confocal laser endomicroscopy

Yu Feng[1,§], Jiali Chen[2,§], Yong Wan[3], Xiaoxiao Ma[3], Bin Zhang[3], Fang Chen[4], Yingwei Fan[2,*], Hongen Liao[1,4,*]

[1] School of Biomedical Engineering, Tsinghua University, Beijing, China;
[2] School of Medical Science and Engineering, Beijing Institute of Technology, Beijing, China;
[3] Viestar (Suzhou) Medical Technology Co., Ltd., Suzhou, Jiangsu, China;
[4] School of Biomedical Engineering and the Institute of Medical Robotics, Shanghai Jiao Tong University, Shanghai, China.

SUMMARY: Confocal laser endomicroscopy (CLE) is a critical modality for the early, minimally invasive diagnosis of intraluminal diseases. However, its clinical translation is constrained by the inherent optical-mechanical trade-offs between numerical aperture (NA), probe diameter, and clinical maneuverability. Achieving high-performance imaging within the strict dimensional limits of standard biopsy channels remains a significant technical bottleneck. To address these challenges, we propose a clinically constrained optical design strategy. This integrated design approach incorporates anatomical boundary constraints directly into the optical optimization process. Based on this method, the developed miniature immersion objective achieved a 0.78 μm lateral resolution across a 300 μm field of view, while the integrated pCLE probe maintained a 1.1 μm lateral resolution. This system realizes stable cellular-level imaging under constrained geometry. It is bending-compatible and clinically deployable. Animal experiments and representative histology-correlated clinical gastric images demonstrated the feasibility of resolving tissue microstructures and clinically relevant mucosal abnormalities, supporting the translational potential of the integrated pCLE probe.

Keywords: optical biopsy, gastric neoplasia, fluorescence microendoscopy, fiber-bundle imaging, translational validation

1. Introduction

Confocal laser endomicroscopy (CLE) has emerged as a pivotal modality for early, minimally invasive diagnosis of intraluminal diseases by enabling real-time, cellular-level optical biopsies. In clinical practice, probe-based CLE (pCLE) is the dominant implementation. Because this probe must simultaneously navigate narrow anatomical channels and acquire microscopic images, the diagnostic capability of pCLE is fundamentally limited by the optical and mechanical performance of the probe (*1,2*).

The clinical utility of pCLE is fundamentally governed by an inherent optical-mechanical trade-off. Specifically, there exists a persistent conflict between achieving a high numerical aperture (NA) for resolution, maintaining millimeter-scale miniaturization for channel compatibility, and ensuring clinical maneuverability for navigating tortuous anatomical paths. This inherent contradiction remains the primary barrier to achieving high fidelity imaging in deep or curved intraluminal environments. (*3-7*).

Existing miniaturization strategies generally fall into three compromised frameworks. First, designs prioritizing anatomical compatibility typically restrict the probe diameter to fit standard biopsy channels, which severely limits the NA (typically ≤ 0.5) and constrains fluorescence collection efficiency (*8-10*). Second, architectures maximizing optical performance (NA ≥ 0.6) often result in bulky outer diameters or extended rigid lengths, precluding safe navigation through tight bending radii (*11*). Third, efforts to mitigate rigidity through mechanically compliant designs, such as flexible gradient-index (GRIN) relays or distal scanning units, often introduce secondary trade-offs including optical path perturbations during bending or increased safety risks from distal actuation (*12-18*). Consequently, a systematic approach to decoupling clinical

maneuverability from optical degradation remains an unresolved challenge.

To address these translational challenges, we propose a clinically constrained optical co-design framework. Unlike traditional sequential design approaches, this method incorporates anatomical boundaries such as biopsy channel diameter, bending radius, and liquid-immersion conditions as practical boundary conditions from the early stage of optical design. By co-optimizing the optical power distribution and mechanical packaging limits, we developed a 5E4G (five-element, four-group) coaxial hybrid architecture. This design provides a practical route for developing high-performance micro-optical systems while preserving maneuverability and anatomical accessibility in clinical applications.

2. Materials and Methods

2.1. Integrated design approach

The core of our methodology is an integrated design approach. This approach maps clinical requirements directly into optical and mechanical design variables. It achieves a dynamic balance among physical laws, manufacturing tolerances, and biological application requirements (Supplementary Materials 1, *https://www.biosciencetrends.com/action/getSupplementalData.php?ID=304*).

We first define a Requirement Vector (R_s) based on clinical benchmarks for cellular-level imaging, which incorporates spectral characteristics, target lateral resolution, working distance, and mechanical constraints dictated by the standard biopsy channel geometry and tissue immersion environments. Correspondingly, an Optical Design Vector (D_s) is established to represent the tunable parameters of the objective, linking R_s and D_s through a series of interconnected physical constraints rather than traditional sequential methods. Within this method, the object-side NA and system magnification are derived from the Nyquist sampling limit of the specific imaging fiber bundle, while the maximum clear aperture of the lens elements is explicitly limited by the barrel wall thickness and biopsy channel diameter to ensure mechanical navigability. Furthermore, high-efficiency fiber coupling is promoted by prioritizing the minimization of the image-side RMS spot radius ($R_{RMS} < d_{core}/2$, where $d_{core}/2$ is the fiber core diameter) over traditional Modulation Transfer Function (MTF) criteria, while the requirements of chromatic aberration and field curvature residuals are related to the system's depth of focus. Finally, these constraints were considered together during optimization to balance high-fidelity imaging with anatomical accessibility.

2.2. pCLE system and miniature objective design

The pCLE system mainly consists of a confocal scanning unit and a confocal imaging probe (Figure 1; detailed supplementary explanation is provided in Supplementary Materials 2, *https://www.biosciencetrends.com/action/getSupplementalData.php?ID=304*). Excitation laser (488 nm) is relayed through a dichroic mirror and optical scanner into a Fujikura FIGH-S series imaging fiber bundle (Fujikura Ltd., Tokyo, Japan). The distal end features a novel miniature fiber-coupled fluorescence microscope objective (hereinafter referred to as the miniature objective) designed to focus the light onto the tissue surface, collect the emitted fluorescence and guide the signal back through the coupling optics for subsequent detection. The optical characteristics are

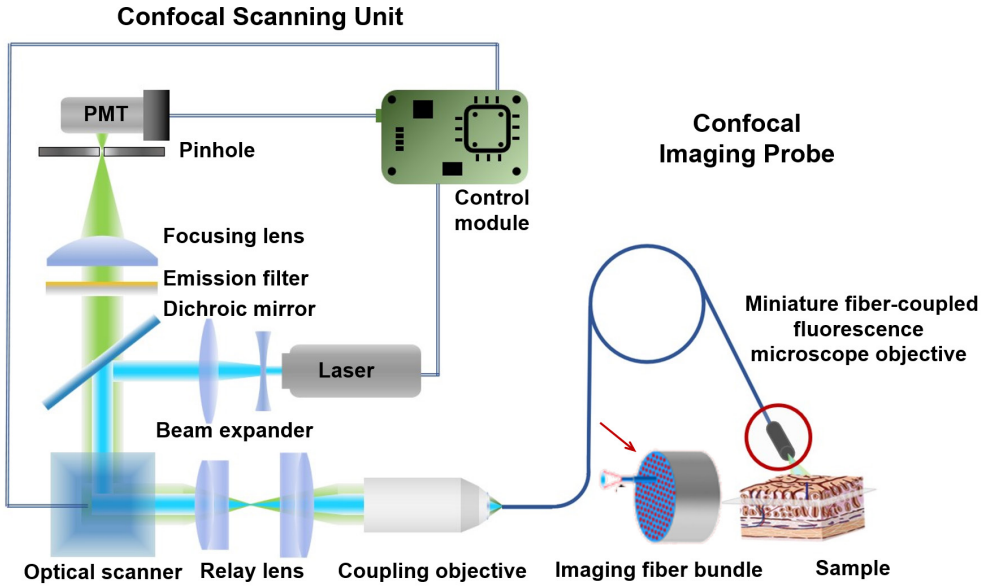

Figure 1. Schematic diagram of the pCLE System.

strictly matched to the properties of sodium fluorescein, a clinically prevalent contrast agent (*19*).

Considering that the probe needs to implement contact imaging, we take seawater to accurately characterize the biological tissue environment(*20*). For contact-mode pCLE imaging, the working distance defines the nominal focal plane beneath the distal optical window and is closely related to the effective imaging depth in superficial gastrointestinal mucosa. Reported pCLE systems using 488-nm excitation and intravenous fluorescein typically generate optical sections at approximately 55-70 μm, while comparable miniature confocal objectives have adopted working distances (WD) of approximately 60-80 μm. Therefore, a WD of 65 μm was selected to position the focal plane within the superficial mucosal layer, enabling visualization of epithelial architecture and cellular-level features while maintaining high-NA fluorescence collection efficiency and compact probe geometry (*3,11,14*) This selection also reflects the general trade-off in turbid biological tissues, where excessive imaging depth can increase scattering-induced degradation of contrast and signal-to-noise ratio (*21*). The miniature objective employs a custom five-element, four-group (5E4G) coaxial hybrid architecture (Figure 2; detailed supplementary explanation is provided in Supplementary Materials 3, *https://www.biosciencetrends.com/action/getSupplementalData.php?ID=304*), designed and optimized using Zemax OpticStudio. The lenses were fabricated using optical glasses sourced from Chengdu Guangming (CDGM Glass Co., Ltd., Chengdu, China). The object-side NA is 0.7, magnifying a 280 μm field of view (FOV) by 2.5× to match the fiber bundle's image circle (3.3 μm core pitch, ~2 μm core diameter). The mechanical outer diameter is strictly limited to 2.6 mm to ensure compatibility with standard 2.8 mm gastrointestinal endoscope working channels (*9,22,23*), with a final rigid mechanical length of 9.1 mm (Figure 2). Within reasonable machining and assembly tolerance ranges (such as sub-ten-micrometer axial errors and tilt errors of less than 0.5°), the system's primary imaging performance metrics remain stable, exerting no significant impact on fiber-coupled imaging. Optical simulations confirm that the objective achieves diffraction-limited performance, featuring an RMS spot radius below 1.0 μm, an MTF exceeding 0.5 at the 151 lp/mm Nyquist frequency, a maximum chromatic focal shift of 3.0 μm, and over 90% uniform relative illumination across the 280 μm field of view. Detailed optical comprehensive performance metrics such as spot diagrams (Supplementary Figure S1, *https://www.biosciencetrends.com/action/getSupplementalData.php?ID=304*), MTF (Supplementary Figure S2, *https://www.biosciencetrends.com/action/getSupplementalData.php?ID=304*), and various aberration curves (Supplementary Figure S3, *https://www.biosciencetrends.com/action/getSupplementalData.php?ID=304*), are provided in the Supplementary Materials.

2.3. Multi-level performance characterization

To verify the efficacy of the constraint-driven design, the fabricated objective underwent rigorous optical and mechanical evaluations. Physical dimensions of the fabricated objective were verified using a high-precision digital micrometer prior to assembly. Under deionized water immersion, lateral resolution and effective FOV were characterized using a standard USAF 1951 resolution test chart and an 80 lp/mm Ronchi grating, respectively. Distortion was analyzed *via* a 10 μm pitch grid distortion target. Furthermore, mechanical navigability and imaging stability were experimentally assessed under physical bending conditions. The integrated probe, with a distal length of 11.48 mm, underwent passability testing within the working channel of a standard electronic endoscope deflected to a maximum mechanical limit, corresponding to a bending radius of 30 mm. To evaluate imaging reliability under mechanical stress, a portion of the probe was coiled around a custom test fixture at a bending radius of 35 mm. This characterization serves to validate that the pre-defined clinical constraints were successfully translated into the final mechanical-optical assembly without

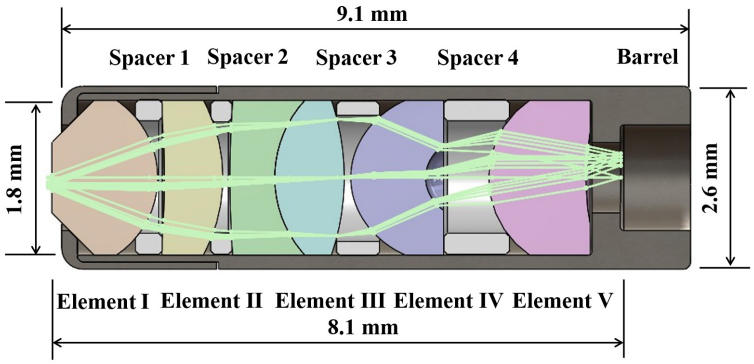

Figure 2. Optical and Mechanical Structure of the Miniature Fiber-Coupled Fluorescence Microscope Objective.

compromising clinical navigability.

2.4. Biological and clinical imaging protocols

To evaluate the biological imaging capability and translational feasibility of the integrated pCLE system, validation experiments were performed using SD rat tissues, an *in vivo* Bama miniature pig bladder model, and representative histology-correlated clinical gastric images. Sodium fluorescein was used as the fluorescence contrast agent. During imaging, the probe tip was gently placed in contact with the target tissue surface while avoiding excessive compression-induced deformation. pCLE images and dynamic video sequences were stored for subsequent comparison with histopathological findings.

For small-animal validation, SD rat colonic mucosa and tibialis anterior muscle/superficial fascia were examined. For colonic mucosal imaging, adult male SD rats were anesthetized by intraperitoneal injection of 10% chloral hydrate solution at 3 mL/kg. Sodium fluorescein solution was then administered *via* the tail vein at a dose of 30 mg/kg. After laparotomy, the colorectum was separated and exposed. An approximately 10-cm colorectal segment was excised, opened longitudinally, and flat-mounted on a glass slide with the mucosal surface facing upward. Intestinal contents were removed, and the mucosal surface was moistened with 0.9% sodium chloride solution. pCLE imaging was performed immediately, with particular attention to colonic crypt architecture and cellular-level mucosal structures.

For tibialis anterior muscle and fascia imaging, adult male SD rats were anesthetized by intramuscular ketamine at 0.3 mL/kg followed by intraperitoneal propofol at 10 mg/kg for continued sedation. The right lower limb was shaved, and the tibialis anterior region was dissected layer by layer to expose the skin, superficial fascia, deep fascia, and tibialis anterior muscle. Sodium fluorescein was locally applied to the exposed tissue surface. Based on preliminary optimization of the staining protocol, pCLE imaging was initiated approximately 30 s after local fluorescein application and completed within 20 min. Images and videos were acquired from the tibialis anterior muscle and superficial fascia, focusing on muscle fiber morphology, intermuscular microvessels, vascular perfusion, and fascia-associated microstructures. After imaging, tissue samples corresponding to the pCLE imaging sites were harvested for histological examination.

For large-animal validation, *in vivo* bladder imaging was performed in a Bama miniature pig model. The animal was fasted for 12-24 h before surgery. Atropine sulfate was administered intramuscularly at 0.05 mL/kg, followed by Zoletil 50 at 0.1 mL/kg for anesthesia induction. After loss of consciousness and attenuation of the corneal reflex, endotracheal intubation was performed, and anesthesia was maintained with isoflurane. An ear-vein catheter was established for intraoperative drug administration, fluid infusion, and sodium fluorescein injection. The bladder was surgically exposed through a midline abdominal incision. Approximately 1 min after intravenous injection of 10% sodium fluorescein, the pCLE probe was gently placed on the bladder mucosa and muscular layer to acquire real-time images and videos. After completion of imaging, the animal was euthanized under deep anesthesia by rapid intravenous injection of potassium chloride. Tissue samples were collected from the corresponding probe-contact sites for histological comparison.

Clinical gastric pCLE images were obtained from a prospective, single-center observational study conducted at the Digestive Endoscopy Center of Guangdong Second Provincial General Hospital. This prospective single-center study included a small patient cohort for feasibility evaluation. Eligible participants were patients aged 20-70 years who presented with digestive symptoms, were suitable for and willing to undergo gastric pCLE examination and provided written informed consent. Patients were excluded if they had a history of gastric surgery; severe cardiac, hepatic, or renal dysfunction that could preclude anesthesia, endoscopy, surgery, or sodium fluorescein metabolism; current anticoagulant or antiplatelet therapy or coagulation disorders that could preclude biopsy; radiological evidence of lymph-node metastasis; pregnancy or lactation; allergic constitution or known sodium fluorescein allergy; or psychiatric conditions preventing cooperation with the study procedures. Before examination, patients fasted for at least 12 h and abstained from water for at least 4 h. Anesthesia risk was evaluated, and an oral defoaming agent and lidocaine were administered 10 min before endoscopy. A sodium fluorescein allergy test was performed before pCLE imaging.

During the clinical procedure, a high-resolution upper gastrointestinal endoscope was first used to inspect the stomach and identify suspicious lesions. The pCLE probe was then advanced through the endoscopic biopsy channel. The probe tip was first placed perpendicular to the adjacent normal mucosa and subsequently moved to the suspicious lesion for pCLE image acquisition. Targeted biopsy, endoscopic resection, or surgical specimens were obtained from the corresponding sites when clinically indicated. The pCLE examination was performed by experienced endoscopists with at least 5 years of pCLE experience. In the present manuscript, the clinical images were used as representative histology-correlated examples of gastric antral high-grade intraepithelial neoplasia and adenocarcinoma rather than for independent diagnostic-accuracy analysis.

For both animal and clinical specimens, tissues corresponding to the pCLE imaging sites were fixed in formalin, embedded in paraffin, sectioned, and stained with hematoxylin and eosin. Histological

sections were reviewed by experienced pathologists and compared with the matched pCLE images to evaluate the correspondence between optical features and tissue microstructures. Representative pCLE images were analyzed descriptively using gray-value histograms and line-intensity profiles to assess image contrast, dynamic range, and structural visibility.

2.5. Ethical approval

All SD rat procedures were approved by the Ethics Committee of Beijing Institute of Technology (Ethics Approval No.: BIT-EC-SCXK2016-0006-M-2021067). The Bama miniature pig experiment was approved by the Institutional Animal Care and Use Committee of Hubei Tianqin Biotechnology Research Institute Co., Ltd. (Approval No.: IACUC-YJY-2024-025). The clinical study was approved by the Medical Ethics Committee of the Second People's Hospital of Guangdong Province (Ethics Approval No.: 2023-KY-KZ-296-02). Written informed consent was obtained from all participants before enrollment, and the clinical study was conducted in accordance with the Declaration of Helsinki.

3. Results

3.1. Optical performance of the miniature objective

The fabricated miniature objective achieves high structural compactness with a length of 9.08 mm and a maximum outer diameter of 2.59 mm (Supplementary Figure. S4, *https://www.biosciencetrends.com/action/getSupplementalData.php?ID=304*). These dimensions confirm that the design is fully compatible with the standard 2.8 mm biopsy channel while maintaining adequate clearance for the pCLE probe.

As shown in Figure 3 (A), in the resolution image obtained with the miniature objective, the finest distinguishable target in the entire imaging area was Group 9, Element 3, corresponding to a lateral resolution of 0.78 μm. This result is sufficient to resolve the detail of imaging fiber pitches for a pCLE probe. As shown in Figure 3 (B), approximately 24-line pairs are visible across the entire imaging area when observing the 80 lp/mm Ronchi grating, yielding an object-side FOV diameter of 300 μm. This measured FOV not only successfully fulfills the rigorous 280 μm design specification but also delivers an extended spatial margin for mechanical tolerance. Figure 3 (C) is the resolution image obtained with our resolution test system alone. By comparing the dimension of the same target (*e.g.*, Group 6, Element 2 in (A) and (C)), the imaging magnification of the miniature objective is calculated to be 2.5x, demonstrating perfect agreement with the theoretical optical design target. Figure 3 (D) shows the measured working distance of the miniature objective, averaging 64.6 ± 3.8 μm across five samples. This minor deviation remains strictly within the acceptable tolerance range and thoroughly satisfies practical application requirements. Finally, the measured MTF curve (Figure 3 (E)) demonstrates the miniature objective's contrast transfer capability. At the system's Nyquist frequency of 151 lp/mm, the miniature objective achieves an MTF value greater than 0.5 in the vertical orientation and 0.6 in horizontal orientation. As shown in Figures 3 (F) and (G), the relative illumination remains above 90% across the entire FOV, satisfying the design specifications. As shown in Figure 3 (H), negligible distortion was observed, which is consistent with theoretical design.

3.2 Probe integration and navigability in a bent endoscopic channel

3.2.1. Probe-level optical performance after integration

Following system integration, the distal rigid length of the complete pCLE probe is 11.48 mm (Figure 4 (A)). The mechanical length is reduced compared to that of the Mauna Kea Technologies (MKT) gastrointestinal probe, which is reported in the literature to be 14 mm (*12*). This miniaturization is a direct result of the integrated design approach that prioritizes distal rigid length as a primary design variable to enhance clinical passability in tortuous anatomical channels.

To evaluate the imaging efficacy of the proposed high-NA architecture, the USAF 1951 resolution target was used. Our probe resolved Group 8, Element 6, corresponding to a lateral resolution of 1.1 μm (Figure 4 (B)). Beyond the resolution target, the integrated probe provided clear visualization of cellular morphology during *ex vivo* rat colon imaging (Figure 4 (C)). Figure 4 (D) shows that approximately 19-line pairs were visible across the field, translating to an effective FOV diameter of ~240 μm. This enhancement is consistent with the high-NA (0.7) optical design employed in this work. It provides high luminal adaptability and effectively elevates the signal floor in biological tissues. These results validate that the integrated design approach achieves an optimal balance between high optical fidelity and the physical constraints inherent to fiber-coupled systems.

3.2.2. Clinical navigability and imaging stability under bending constraints

To validate the translational value of the clinically constrained design, we evaluated the mechanical passability and optical performance stability of the integrated probe under severe bending conditions. We assessed the navigability of the probes within the working channel of a standard electronic endoscope (Model: GIF-H180J, Olympus). The proposed probe, benefiting from its optimized distal rigid length, successfully navigated through the endoscopic

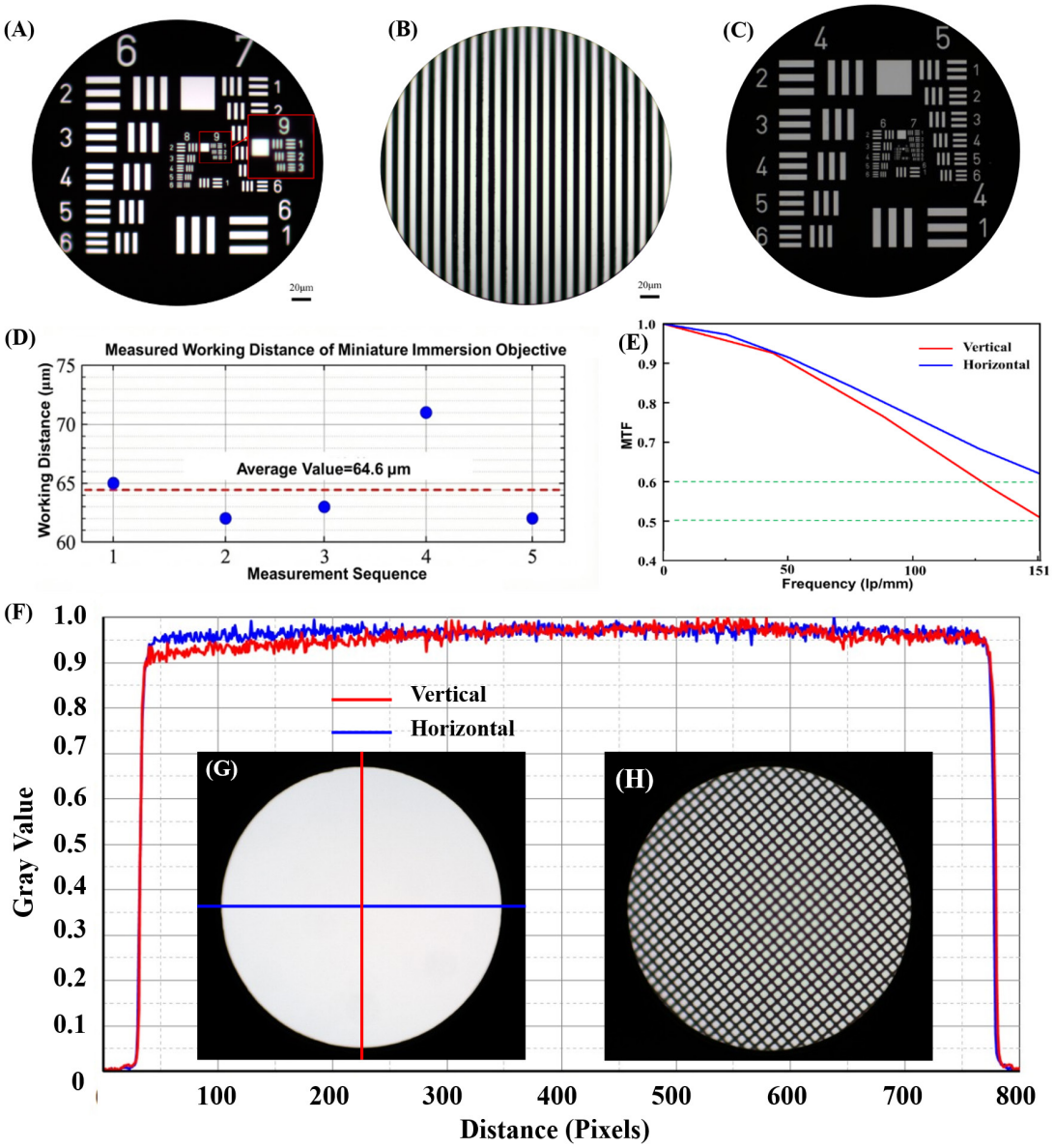

Figure 3. Optical Performance Characterization of the Miniature Fiber-Coupled Fluorescence Microscope Objective. (A) Image of the USAF 1951 Resolution Test Chart with miniature objective; **(B)** Image of the Ronchi Grating Test Plate; **(C)** Image of the USAF 1951 Resolution Test Chart with our resolution test system only; **(D)** Measured Working Distance of Miniature objective; **(E)** MTF Measurement Curve of the Miniature objective; **(F)** Relative illumination measurement results; **(G)** Original image of relative illuminance; **(H)** Distortion measurement results.

channel even when the endoscope tip was deflected to its maximum mechanical limit, corresponding to a limit bending radius of 30 mm (Figure 4 (E)). This passability test directly confirms that our design improves the probe maneuverability in complex luminal geometries.

Beyond physical passability, image degradation caused by probe deformation during clinical maneuvers represents a fundamental challenge in pCLE. Because conventional static evaluations may not fully reflect these conditions, we used a bending stress-test method to evaluate imaging stability under clinically relevant mechanical deformation. Imaging stability was evaluated with a portion of the probe coiled around a custom fixture with a rigorous bending radius of 35 mm (Figure 4 (F)). Under this condition, the resolution target imaging confirmed that the lateral resolution remained stable at 1.1 μm (Figure 4 (G)). Furthermore, *ex vivo* rat colon imaging acquired under the bending state revealed no discernible loss of cellular detail or architectural contrast compared with the unbent configuration (Figure 4 (H)). By aligning optical validation directly with clinical reality, this problem-driven methodology provides critical evidence for the probe's translational viability. These results confirm that the proposed probe successfully passed through the endoscope working channel at a bending radius of 30 mm. Under a bending radius of 35 mm, the proposed probe maintained a

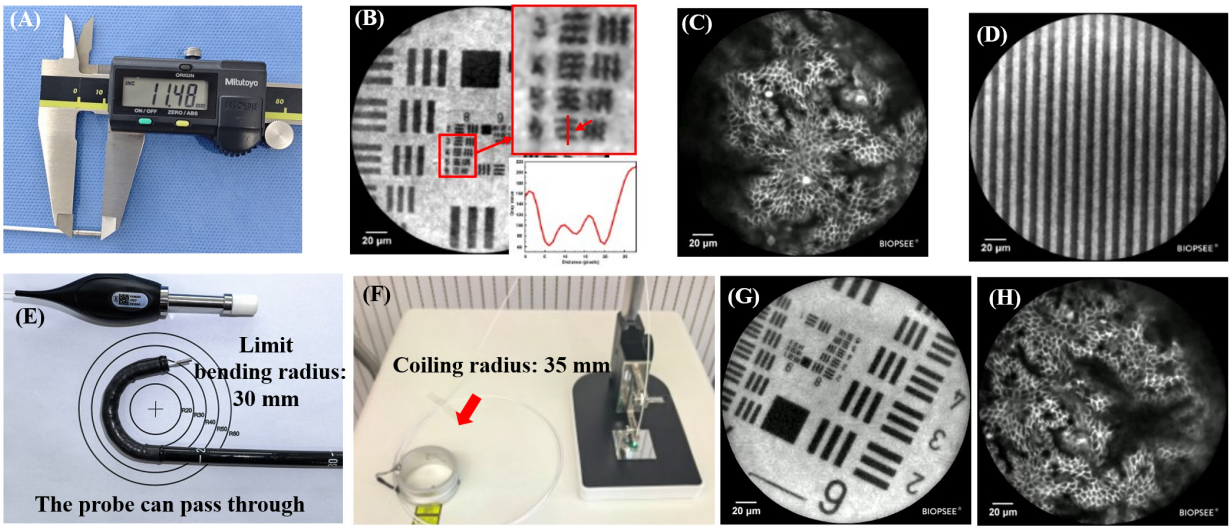

Figure 4. Probe-Level Optical Performance and Bending-Compatible Endoscopic Navigability of the Integrated pCLE System. (A) The distal rigid length of the complete pCLE probe; **(B)** Resolution test chart of the complete pCLE probe; **(C)** *Ex vivo* rat colon imaging of the complete pCLE probe; **(D)** Image of the Ronchi Grating Test Plate. **(E)** The proposed probe successfully passing through the endoscope channel bending at a radius of 30 mm; **(F)** Experimental setup for evaluating imaging stability with a portion of the probe coiled at a 35 mm radius; **(G)** Resolution Target image acquired under the 35 mm bending configuration; **(H)** *Ex vivo* Rat Colon image at the 35 mm bending configuration. (The limit bending radius is defined as the smallest radius of the electronic endoscope's distal bending section when the deflection control knob is rotated to its maximum extent).

Table 1. Parameter Comparison

Specification Items	Yang L (*9*)	Li H (*14*)	Lu T (*11*)	Rouse A R (*15*)	Kyrish M (*10*)	Ours
Object						
Wavelengths (nm)	488-550	488-550	488-550	480-660	452-623	488-600
Magnification	2	2.2	2	1.6	2	2.5
Object-side NA	0.5	0.52	0.6	0.46	0.55	0.7
Working distance (μm)	150	80	60	0-200	15	64.6 ± 3.8
Object-side FOV (μm)	360	570	600	450	360	300
RMS Radius (μm)	< 1.2	< 2	< 2	< 3	/	< 1.0
MTF@Nyquist Frequency (lp/mm)	> 0.5@167	> 0.5@132	>0.5@132	> 0.5@166	/	> 0.5@151
Clear Aperture (mm)	1.4	1.8	3	1.6	1.5	1.8
Mechanical Length (mm)	/	11.2	21	13	/	9.1
Outer Diameter (mm)	2.6	2.6	4.6	3	2.1	2.6
Number of Elements	4	6	5	6	6	5
Probe						
Lateral resolution (μm)	1.55	1.95	1.95	/	2.19	1.10
Distal rigid length (mm)	10.3	/	/	/	/	11.48
FOV	/	512.5μm	540 μm	/	/	240 μm
Dynamic bending validation	Not reported	Not reported	Not reported	Not reported	Not reported	Validated
Endoscopic channel compatibility under extreme bending	Not reported	Not reported	Not reported	Not reported	Not reported	Validated

/ Refers to the lack of information or detailed numerical values provided.

lateral resolution of 1.1 μm and preserved cellular-level imaging quality with no discernible degradation compared to the unbent configuration.

A comparative analysis of the specifications between our design and existing designs is presented in Table 1. A comprehensive assessment of critical metrics (including NA, Total Mechanical Length, Magnification, and RMS radius) demonstrates that our design achieves a favorable engineering balance among high NA, compact outer diameter, short distal rigid length, and cellular-level resolution, establishing it as a viable solution for pCLE applications that balances high imaging performance with clinical navigability.

3.3. Tissue imaging

3.3.1. Imaging of rat colon and tibialis anterior muscle

In rat colonic mucosa, the pCLE system clearly visualized crypt-like glandular architecture and

cellular-level epithelial structures (Figures 5 (A) and 5 (B)). The glandular openings, epithelial lining, and luminal boundaries were distinguishable, indicating sufficient contrast for resolving superficial mucosal microstructures. Line-intensity and gray-value analyses further showed clear signal differences between crypt structures and surrounding tissue without obvious signal saturation (Figures 5 (C) and 5 (D)).

In tibialis anterior muscle, pCLE images showed elongated hypointense muscle fibers separated by hyperintense intermuscular microvessels (Figures 6 (A) and 6 (B)). Dynamic imaging further allowed visualization of microvascular perfusion. The corresponding histological section confirmed the parallel arrangement of skeletal muscle fibers (Figure 6 (C)). In the superficial fascia, pCLE visualized elliptical adipocyte-like structures and interlacing vascular networks (Figures 6 (D) and 6 (E)), which were consistent with the adipose and fibrous components observed on histology (Figure 6 (F)). Gray-value histograms of representative images showed variable contrast among muscle, vascular, and fascial structures without obvious signal saturation (Figures 6 (G-J)).

3.3.2. Imaging of bama miniature pig bladder

In the Bama miniature pig bladder model, the integrated pCLE system visualized urothelial, vascular, and muscular structures *in vivo* (Figures 7 (A), 7 (C), 7(E), and 7 (G)). Capillary networks in the lamina propria and fiber-bundle-like structures in the muscular layer were distinguishable, and flowing blood cells could be observed during dynamic imaging. Matched histological sections confirmed the presence of urothelium, loose connective tissue, vascular structures, and smooth muscle layers corresponding to the pCLE findings (Figures 7 (B), 7 (D), 7 (F), and 7 (H)). Gray-value histograms of representative images showed tissue-dependent contrast patterns, supporting the ability of the probe to distinguish heterogeneous bladder microstructures (Figures 7 (I-L)).

3.3.3. Imaging of human antrum

Representative clinical pCLE images of gastric antral HGIN and adenocarcinoma showed histology-correlated abnormalities, including reduced glandular

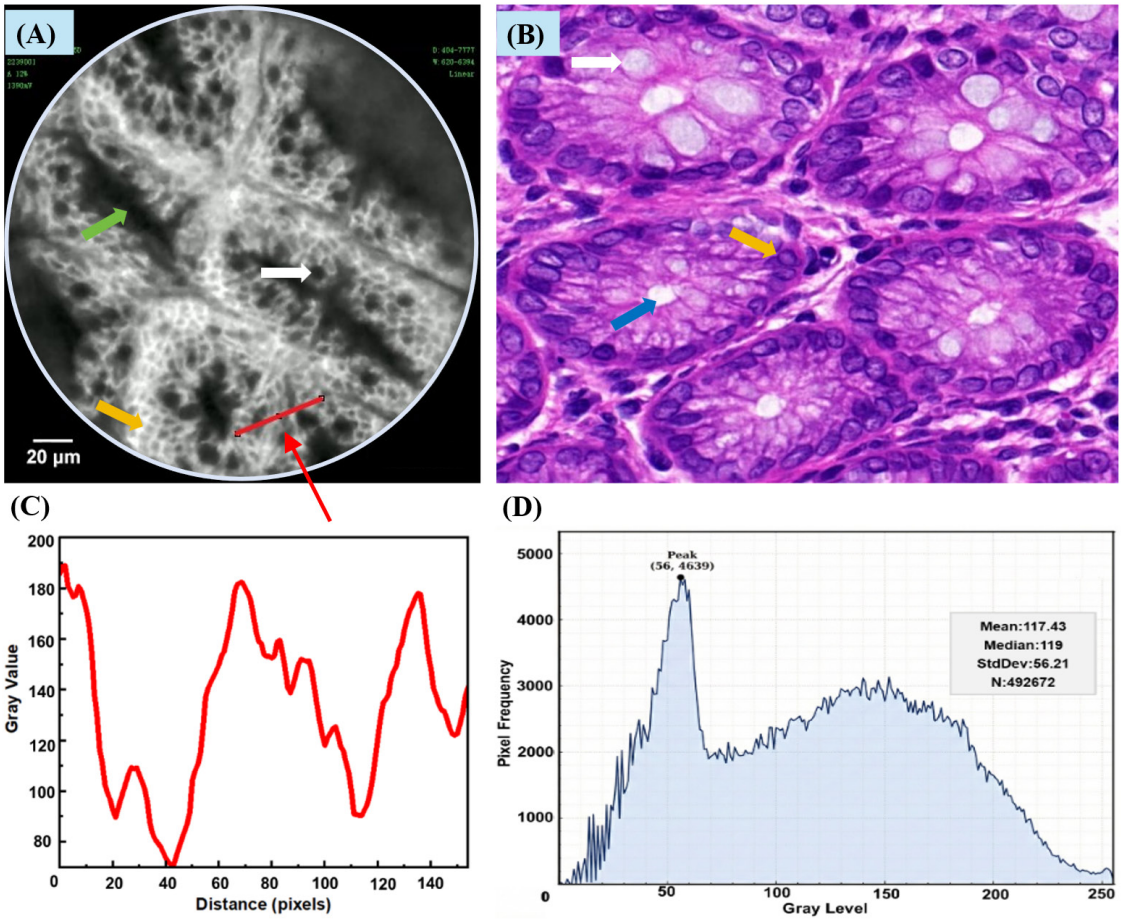

Figure 5. *Ex vivo* Imaging of Rat Colonic Mucosa. (A) Confocal Laser Endomicroscopic Image of Colonic Mucosa. This demonstrates the capability to resolve cellular level mucosal structures; **(B)** Histopathological Section of Colonic Mucosa. White arrows: Goblet cells arranged in a chrysanthemum-like pattern within the glands; Green arrows: Central openings of the glands; Yellow arrows: Columnar epithelial cells; Blue arrows: Glandular lumens; **(C)** The line profile of the area marked by the red line in the **(A)**; **(D)** Histograms of gray values in the **(A)**.

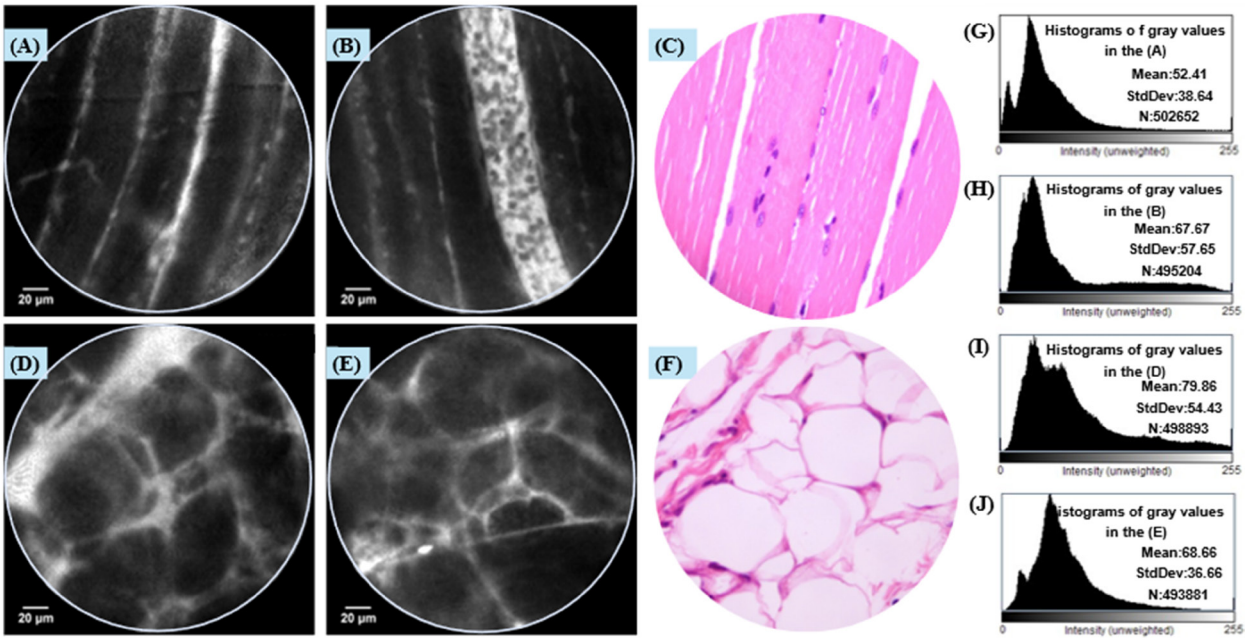

Figure 6. Imaging of the Muscular Layer and Superficial Fascia Layer of Rat Tibialis Anterior Muscle. (A) and **(B)** pCLE Image of the Muscular Layer. These images display excellent microvascular and fibrous structural contrast; **(C)** Histopathological Section of the Muscular Layer; **(D)** and **(E)** pCLE Image of the Superficial Fascia Layer. They exhibit distinct fascial architecture; **(F)** Histopathological Section of the Superficial Fascia Layer; **(G)**, **(H)**, **(I)** and **(J)** Gray-value histograms corresponding to **(A)**, **(B)**, **(D)** and **(E)**, respectively.

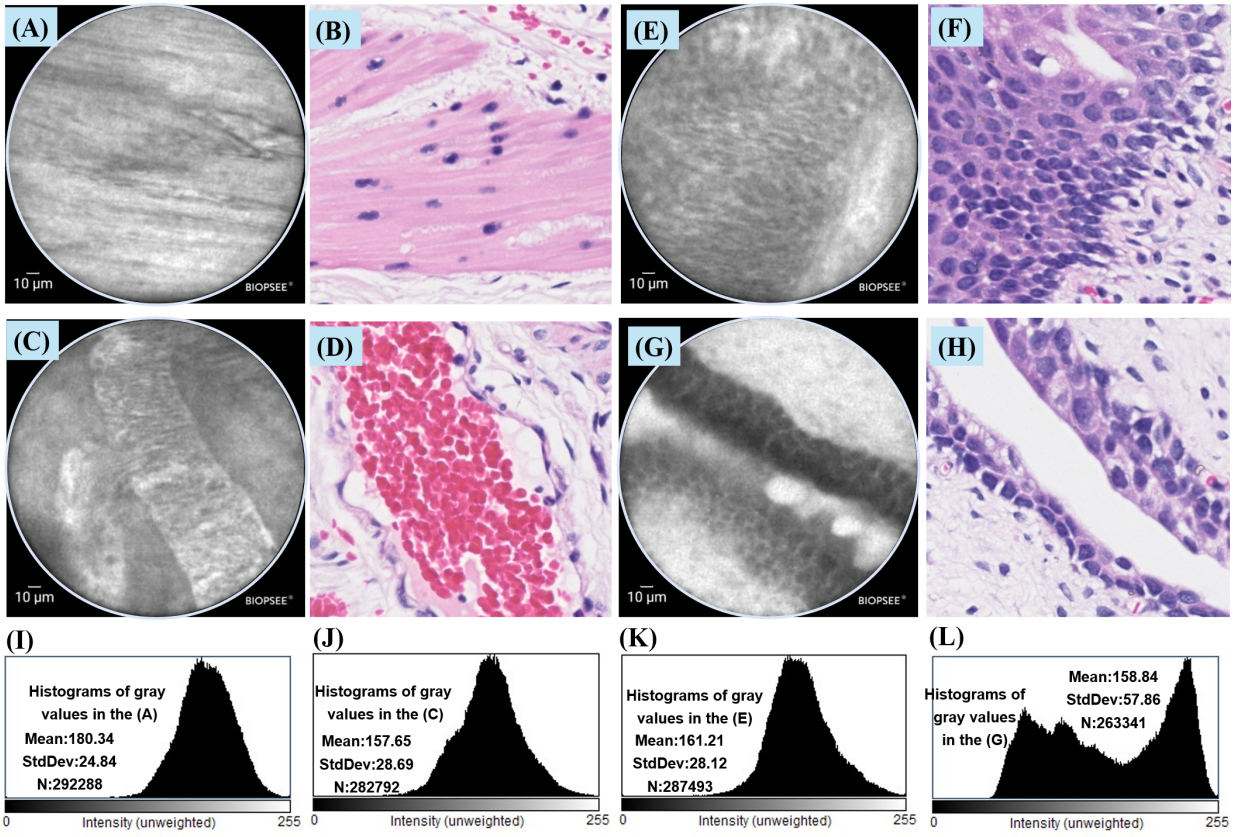

Figure 7. ***In vivo*** **Imaging of Bama Miniature Pig Bladder. (A)** pCLE Image of Muscle Fibers. This confirms the luminal adaptability of the probe in living tissue; **(B)** Histopathological Section of Muscle Fibers; **(C)** pCLE Image of Capillaries; **(D)** Histopathological Section of Capillaries; **(E)**, **(G)** pCLE Images of Epithelial Cells; **(F)**, **(H)** Histopathological Sections of Epithelial Cells; **(I)** **(J)**, **(K)** and **(L)** Gray-value histograms corresponding to **(A)**, **(C)**, **(E)** and **(G)**, respectively.

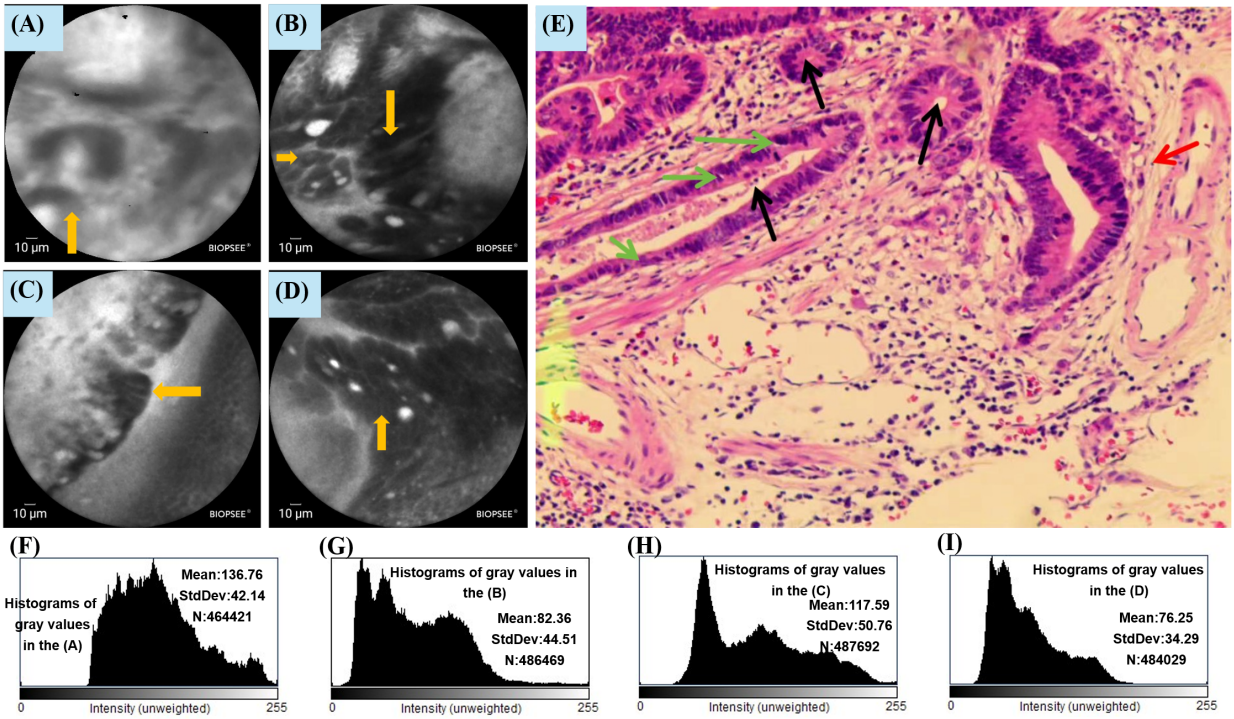

Figure 8. Imaging of Human Gastric Antrum. (A) (B) (C) and **(D)** pCLE Images of High-Grade Intraepithelial Neoplasia (HGIN)-Adenocarcinoma. These are representative histology correlated gastric lesion images. They demonstrate the preservation of glandular structural visibility under clinically constrained probe geometry; **(E)** Histopathological Section. (Yellow arrows: Sparse glandular structures. Green arrows: Epithelial cells. Red arrows: Glandular epithelial structures. Black arrows: Sparse glands); **(F) (G)**, **(H)** and **(I)** Gray-value histograms corresponding to **(A)**, **(B)**, **(C)** and **(D)**, respectively.

density, disrupted glandular architecture, epithelial disorganization, and focal fluorescein leakage (Figures 8 (A-D)). The matched histopathological section confirmed neoplastic epithelial proliferation with glandular architectural distortion and cellular atypia (Figure 8 (E)). Gray-value histograms showed heterogeneous contrast distributions among different fields, reflecting variable glandular architecture, mucus/surface scattering, and fluorescein distribution (Figures 8 (F-I)). These findings demonstrate the feasibility of visualizing clinically relevant gastric mucosal abnormalities with the integrated pCLE probe.

4. Discussion

This study developed and evaluated a clinically constrained miniature immersion objective for pCLE, with the goal of balancing high-NA fluorescence collection, cellular-level resolution, compact distal geometry, and endoscopic navigability. The major finding is that the proposed objective was not only optically feasible as an isolated component but could also be integrated into a probe that retained cellular-level imaging performance under clinically relevant bending conditions. The fabricated objective achieved an object-side NA of 0.7, a 2.6-mm outer diameter, and a 9.1-mm rigid length. After integration, the pCLE probe maintained a lateral resolution of 1.1 µm, an effective FOV of approximately 240 µm, and stable imaging performance during bent-channel testing. The compact distal architecture achieves both high optical performance and clinical accessibility.

These findings hold important translational significance. They address the limitations of existing technologies. Conventional pCLE systems may encounter limitations in anatomically tortuous or highly angulated luminal environments due to distal rigidity and maneuverability constraints. These limitations are particularly relevant in applications requiring stable imaging through sharply bent endoscopic channels. The present design was developed specifically to address this translational bottleneck while preserving cellular-level imaging capability.

The design strategy differs from conventional miniature optical design workflows in that clinical constraints were treated as initial boundary conditions rather than as post-design packaging requirements. For fiber-bundle-based pCLE, optical resolution, FOV, working distance, and magnification must be matched to the discrete sampling properties of the imaging fiber, while the distal optical assembly must remain compatible with standard endoscopic working channels and mechanical bending. In this context, the proposed clinically constrained co-design approach links fiber-bundle sampling, water-immersion contact imaging, endoscopic channel diameter, short rigid-

tip requirements, and bending navigability into a single clinically constrained design. Detailed optical optimization and engineering design procedures are provided in the Supplementary Materials (*https://www.biosciencetrends.com/action/getSupplementalData.php?ID=304*), while the main text focuses on the translational performance of the fabricated and integrated probe.

The present architecture helps mitigate a common trade-off in miniature pCLE probe development. GRIN-lens-based probes can provide favorable flexibility and compactness, but bending-related changes in the optical path may affect image quality in some configurations (*16*). Distal-scanning approaches based on MEMS or piezoelectric actuation can reduce fiber-bundle pixelation and provide continuous scanning images; however, the integration of actuators, driving components, and protective packaging may increase distal complexity, rigid length, and safety requirements (*13,24*). In contrast, the present design uses a passive high-NA distal objective coupled to an imaging fiber bundle. Although this architecture retains the intrinsic sampling limitation and pixelated pattern of fiber-bundle imaging, it provides a mechanically simple and compact solution that is compatible with standard endoscopic access and stable under bending. The 30-mm endoscopic passability test and 35-mm coiling test support the mechanical feasibility of this approach.

The biological imaging results further support the feasibility of the integrated pCLE probe in tissue environments. In freshly excised rat colonic mucosa after systemic sodium fluorescein administration, the system visualized crypt-like glandular architecture and cellular-level mucosal features. In rat tibialis anterior muscle and superficial fascia after local fluorescein application, the probe resolved muscle fiber organization, intermuscular microvascular structures, and fascia-associated adipose and vascular networks. In the Bama miniature pig bladder model, *in vivo* imaging demonstrated distinguishable urothelial, vascular, and muscular features with histological correspondence. These results indicate that the high-NA miniature objective can provide sufficient contrast and structural visibility across epithelial, muscular, vascular, and connective-tissue-rich structures.

The representative clinical gastric images provide preliminary evidence of translational relevance but should be interpreted as histology-correlated feasibility observations rather than diagnostic-accuracy validation. In gastric antral HGIN and adenocarcinoma, pCLE images showed abnormal glandular architecture, epithelial disorganization, reduced glandular regularity, and focal fluorescein leakage, with corresponding histopathological confirmation. These findings suggest that the integrated probe can visualize clinically relevant mucosal abnormalities during endoscopic imaging. However, the present clinical dataset is not sufficient to establish diagnostic sensitivity, specificity, interobserver agreement, or lesion-level diagnostic accuracy. Future clinical studies should therefore include larger patient cohorts, standardized image-quality criteria, blinded image interpretation, and predefined histopathological correlation protocols.

Previous clinical studies have shown that pCLE can provide microscopic information during endoscopy in a range of clinical settings, including pharyngeal neoplasia, Barrett esophagus-associated intestinal metaplasia, esophageal neoplasia, gastric cancer and precancerous lesions, small-bowel diseases, Crohn disease, and selected extra-gastrointestinal applications (*25-35*). These studies collectively support the clinical demand for real-time optical biopsy tools capable of resolving epithelial architecture, cellular atypia, vascular leakage, and glandular organization. Importantly, these prior reports should be viewed as evidence for the broader clinical need and potential utility of pCLE, rather than as direct validation of the miniature objective developed in the present study. The contribution of this work is to address a device-level bottleneck: achieving high-NA, cellular-level imaging while preserving compatibility with standard endoscopic working channels and bent intraluminal navigation.

Several limitations should be acknowledged. First, the ultimate spatial resolution of the integrated pCLE system remains constrained by the core-to-core pitch of the imaging fiber bundle, even though the 0.7-NA objective improves fluorescence collection efficiency. Second, effective FOV is limited by the need to maintain cellular-level resolution within a compact optical design, which may restrict wide-area screening. Third, the current biological and clinical experiments were primarily feasibility and histology-correlation studies. The animal experiments were not designed to evaluate disease-specific diagnostic performance, and the clinical images were not sufficient for formal statistical analysis. Because fluorescein administration routes and tissue environments differed among the animal models, gray-value histograms were used for descriptive image-quality assessment rather than direct quantitative comparison across tissues. Fourth, the present system was optimized for fluorescein-based visible-light imaging; therefore, its performance with other fluorophores, molecular probes, or near-infrared excitation requires further optical and biological validation.

Future work should focus on three directions. First, the integrated probe should be evaluated in larger prospective clinical studies with standardized acquisition protocols, quantitative image-quality metrics, and blind interpretation. Second, the optical design may be further adapted to expand FOV, reduce fiber-bundle artifacts, or improve compatibility with different endoscopic platforms. Third, molecularly targeted contrast agents and near-infrared pCLE may enhance lesion-specific contrast and improve the detection of early-stage disease

at the cellular level (*36*). Such extensions will require optimization of lens transmission, fiber compatibility, fluorescence collection efficiency, and clinical safety. Overall, this study supports the feasibility of a clinically constrained high-NA miniature objective for pCLE and may provide a compact platform for future real-time optical biopsy and molecular endomicroscopy studies.

5. Conclusion

This study developed and validated a clinically constrained high-NA miniature immersion objective for pCLE. The integrated probe achieved cellular-level imaging performance within compact distal geometry and maintained stable imaging under bent-channel conditions. Animal imaging and representative histology-correlated clinical gastric images further supported its feasibility for real-time optical biopsy. Larger prospective clinical studies are needed to determine diagnostic accuracy and clinical utility.

Funding: This work was supported by grants from the National Natural Science Foundation of China (NSFC) under Grant Nos. U22A2051, and 82172112; the National Key Research and Development Program of China under Grant No. 2022YFC2405200; the Henan Science and Technology Development Joint Fund under Grant No. 235200810067; and the Beijing Institute of Technology Research Fund Program for Young Scholars under Grant No. XSQD-202123006.

Conflict of Interest: The authors have no conflicts of interest to disclose.

References

1. Richards-Kortum R, Lorenzoni C, Bagnato VS, Schmeler K. Optical imaging for screening and early cancer diagnosis in low-resource settings. Nat Rev Bioeng. 2024; 2:25-43.
2. Wallace MB, Fockens P. Probe-based confocal laser endomicroscopy. Gastroenterology. 2009; 136:1509-1513.
3. Ayyad M, Gala D, Albandak M, Goyal RM, Abboud Y, Al-Khazraji A, Hajifathalian K. Probe-based confocal laser endomicroscopy: progress, challenges, and emerging applications. Surg Endosc. 2025; 39:7958-7972.
4. Fuks D, Pierangelo A, Validire P, Lefevre M, Benali A, Trebuchet G, Criton A, Gayet B. Intraoperative confocal laser endomicroscopy for real-time *in vivo* tissue characterization during surgical procedures. Surg Endosc. 2019; 33:1544-1552.
5. Sagar Shrikrishna NS, Sharma R, Sahoo J, Kaushik A, Gandhi S. Navigating the landscape of optical biosensors. Chemical Engineering Journal. 2024; 490. doi: 10.1016/j.cej.2024.151661.
6. Chen J, Liu S, Gao T, Tang X, Liao H, Fan Y. Research progress on endoscopic multimodal optical imaging. Optics & Laser Technology. 2025; 191. doi: 10.1016/j.optlastec.2025.113355.
7. Rothermel F, Toulouse A, Thiele S, Jung C, Drozella J, Steinhoff R, Giessen H, Herkommer AM. Magnetically actuatable 3D-printed endoscopic microsystems. Commun Eng. 2025; 4:69.
8. Li G, Duan X, Lee M, Birla M, Chen J, Oldham KR, Wang TD, Li H. Ultra-Compact Microsystems-Based Confocal Endomicroscope. IEEE Trans Med Imaging. 2020; 39:2406-2414.
9. Yang L, Wang J, Tian G, Yuan J, Liu Q, Fu L. Five-lens, easy-to-implement miniature objective for a fluorescence confocal microendoscope. Opt Express. 2016; 24:473-484.
10. Kyrish M, Dobbs J, Jain S, Wang X, Yu D, Richards-Kortum R, Tkaczyk TS. Needle-based fluorescence endomicroscopy *via* structured illumination with a plastic, achromatic objective. J Biomed Opt. 2013; 18:096003.
11. Lu T, Li H, Zhang W, Deng Y, Liu Q, Fu L. A handheld confocal microendoscope compatible with laparoscopy for histology in situ. Optics and Lasers in Engineering. 2023; 164.
12. Ford TN. Fast widefield techniques for fluorescence and phase endomicroscopy. Boston University, 2013. https://open.bu.edu/items/eee46d91-bf48-4af7-8e95-77901355166a (accessed May 5, 2026).
13. Lee M, Li G, Li H, Duan X, Birla MB, Chang TS, Turgeon DK, Oldham KR, Wang TD. Confocal laser endomicroscope with distal MEMS scanner for real-time histopathology. Sci Rep. 2022; 12:20155.
14. Li H, Hao Z, Huang J, Lu T, Liu Q, Fu L. 500 μm field-of-view probe-based confocal microendoscope for large-area visualization in the gastrointestinal tract. Photonics Research. 2021; 9:1829-1841.
15. Rouse AR, Kano A, Udovich JA, Kroto SM, Gmitro AF. Design and demonstration of a miniature catheter for a confocal microendoscope. Appl Opt. 2004; 43:5763-5771.
16. Liu G, Kang JW, Bhagavatula S, Ahn SW, So PTC, Tearney GJ, Jonas O. Bendable long graded index lens microendoscopy. Opt Express. 2022; 30:36651-36664.
17. Chen X, Yan S, Wu Y, Jia G, Xia K, Guan Y, Shen X, Wang X, Dai S, Shen X, Liu Z. Fabrication and performance of high refractive index achromatic gradient index chalcogenide glass. Opt Express. 2025; 33:7841-7851.
18. Huland DM, Brown CM, Howard SS, Ouzounov DG, Pavlova I, Wang K, Rivera DR, Webb WW, Xu C. *In vivo* imaging of unstained tissues using long gradient index lens multiphoton endoscopic systems. Biomed Opt Express. 2012; 3:1077-1085.
19. Xu R, Teich W, Frenzel F, Hoffmann K, Radke J, Rosler J, Faust K, Blank A, Brandenburg S, Misch M, Vajkoczy P, Onken JS, Resch-Genger U. Optical Characterization of Sodium Fluorescein *In Vitro* and *Ex Vivo*. Front Oncol. 2021; 11:654300.
20. Huang J, Ou Z. Refractive index engineering: Insights from biological systems for advanced optical design. Laser & Photonics Reviews. 2025; 19:e00180.
21. Gu M, Gan X, Deng X. Microscopic Imaging Through Turbid Media: Monte Carlo Modeling and Applications. Springer, Berlin, Heidelberg, Germany, 2015.
22. Han X, Zhu J, Shen W, Zhou P. Optical design of mesoscope objective with high resolution and large field of view. Proc SPIE. 2024; 13104:131042V. doi:10.1117/12.3023250.
23. Tang Y, Kortum A, Vohra I, Othman M, Dhingra S, Mansour N, Carns J, Anandasabapathy S, Richards-Kortum R. Improving nuclear morphometry imaging with real-time and low-cost line-scanning confocal

microendoscope. Opt Lett. 2019; 44:654-657.
24. He L, Li X, Yang J, Jiang L, Liu Q, Fu L. Super-simplified fiber scanner for cellular-resolution endoscopic imaging. Photonics Research. 2023; 11:2020-2032.
25. Chen Y, Zhang Y, Zhao Q, Zhou F, Ge L. Confocal Laser Endomicroscopy in the Diagnosis of Pharyngeal Neoplasms: An Optical Biopsy Approach. Gastrointest Endosc. 2026: S0016-5107(26)00228-2.
26. Ding Y, Song R, Xing J, Cheng R, Yang K, Sun X, Li P, Zhang S. Diagnostic value of probe-based confocal laser endomicroscopy for intestinal metaplasia in Barrett esophageal mucosa. Chin J Dig Endosc,. 43:50-55.
27. Liu J, Cai M, Yang M, Luo J, Zhao Q. Synchronous multiple primary early stage esophageal cancers diagnosed in a teenager using confocal laser endomicroscopy. Endoscopy. 2025; 57:E402-E404.
28. Peng X, Zheng YP, Zhang Y. The benefits of using confocal laser endomicroscopy in the diagnosis of gastric cancer and precancerous lesions: A case report. Front Oncol. 2025; 15:1649985.
29. Shi Y, Zeng Q, Chen Y, Zhou M, Zhang S. The diagnostic value of confocal laser endomicroscopy in a cancer-mimicking lesion. Endoscopy. 2025; 57:E903-E904.
30. Liu J, Song Y, Luo J, Yang P, Shi X, Zhao Q. Confocal laser endomicroscopy for the diagnosis of gastric adenocarcinoma of the fundic gland type. Gastrointest Endosc. 2024; 100:948-949.
31. Dong Z, Tian B, Wu S, Qian Y, Zhuang Q, Wan X. Real-time probe-based confocal laser endomicroscopy visualization of dual differentiation features in mixed-type gastric adenocarcinoma. Endosc Int Open. 2025; 13:a27128674.
32. Fan L, Huang X, Luo J, Yang L, Zhao Q, Liu J. Confocal endoscopy-assisted diagnosis of duodenal follicular lymphoma: A rare case report. Endoscopy. 2025; 57:E560-E561.
33. Ding H, Chen HM, Li XB, Sheng YF, Gong S. Observation study of small bowel diseases by enteroscopy combined with probe-based confocallaser endomicroscopy. Journal of Clinical Internal Medicine. 2024; 41:446-450. (in Chinese)
34. Kai N, Xiaoyan W. A Microscopic Lens for Macroscopic Decisions in the "Non-lifting Sign" of Crohn's Disease. Dig Dis Sci. 2026; doi.org/10.1007/s10620-026-09875-w.
35. Wen J, Yang X, Ye G, Chen R, Feng Y, Liao Q. Preliminary study of confocal laser endomicroscopy for *in vitro* specimens of the endometrium. BMC cancer. 2022; 22:1094.
36. Kennedy GT, Azari FS, Bernstein E, *et al*. Targeted detection of cancer at the cellular level during biopsy by near-infrared confocal laser endomicroscopy. Nat Commun. 2022; 13:2711.

Received April 25, 2026; Revised May 20, 2026; Accepted May 22, 2026.

[§]These authors contributed equally to this work.

*Address correspondence to:
Hongen Liao, School of Biomedical Engineering, Tsinghua University, Beijing 100084, China.
School of Biomedical Engineering and the Institute of Medical Robotics, Shanghai Jiao Tong University, Shanghai, China.
E-mail: liao@tsinghua.edu.cn

Yingwei Fan, School of Medical Science and Engineering, Beijing Institute of Technology, Beijing 100081, China.
E-mail: fanyingwei@bit.edu.cn

Released online in J-STAGE as advance publication June 2, 2026.